
ORGAN: OBJECT-CENTRIC REPRESENTATION LEARNING USING CYCLE CONSISTENT GENERATIVE ADVERSARIAL NETWORKS

Joël Küchler^{a,†}, Ellen van Maren^b, Vaiva Vasiliauskaitė^a, Katarina Vulić^a, Reza Abbasi-Asl^c, and Stephan J. Ihle^{a,d,e,†,✉}

^aLaboratory of Biosensors and Bioelectronics, Institute for Biomedical Engineering, University and ETH Zurich, Gloriastrasse 37/39, Zurich, 8092, Switzerland

^bDepartment of Neurology, Insel Gruppe, Bern, Switzerland

^cDepartment of Neurology, Department of Bioengineering and Therapeutic Sciences, University of California, San Francisco, USA

^dDepartment of Neurobiology, University of Chicago, 951 E 58th St, Chicago, 60637, IL, USA

^eDepartment of Physics, University of Chicago, 929 E 57th St, Chicago, 60637, IL, USA

[†]These authors contributed equally to this work.

[✉]Corresponding author: ihles@uchicago.edu

ABSTRACT

Although data generation is often straightforward, extracting information from data is more difficult. Object-centric representation learning can extract information from images in an unsupervised manner. It does so by segmenting an image into its subcomponents: the objects. Each object is then represented in a low-dimensional latent space that can be used for downstream processing. Object-centric representation learning is dominated by autoencoder architectures (AEs). Here, we present ORGAN, a novel approach for object-centric representation learning, which is based on cycle-consistent Generative Adversarial Networks instead. We show that it performs similarly to other state-of-the-art approaches on synthetic datasets, while at the same time being the only approach tested here capable of handling more challenging real-world datasets with many objects and low visual contrast. Complementing these results, ORGAN creates expressive latent space representations that allow for object manipulation. Finally, we show that ORGAN scales well both with respect to the number of objects and the size of the images, giving it a unique edge over current state-of-the-art approaches.

Keywords CycleGAN · Generative models · Object-centric representation learning · Representation learning.

1 Introduction

Image datasets are ever-increasing in size. Yet, labeling their content remains costly. As a consequence, unsupervised object detection in images is a pressing need in the field of machine learning Pervez et al. [2022], Locatello et al. [2020]. Object-centric representation learning is a powerful tool towards this goal. It focuses on elucidating the presence, location, and properties of objects of a given scene in an unsupervised fashion. As such, it is capable of separating a scene into multiple objects, which are condensed into a latent representation.

Object-centric representations are similar to the way humans reason and make predictions about the physical world Battaglia et al. [2013], Lake et al. [2017], Kubricht et al. [2017], Spelke et al. [1992]. Therefore, it is no wonder that these types of representations are deemed more interpretable Mascharka et al. [2018]. Object-centric representations can be recovered using classical approaches, such as wavelet representations Papageorgiou et al. [1998] and template matching Betke and Makris [1995], as well as using deep learning. Unsupervised techniques are desirable, as they do not require labels but instead focus on intrinsic biases in the data. Two well-known unsupervised classes of architectures that can be used to create representations are variational auto-encoders (VAEs) Kingma [2013] and generative adversarial networks (GANs) Goodfellow et al. [2014]. However, there are also other unsupervised approaches with similar capabilities Kipf et al. [2019].

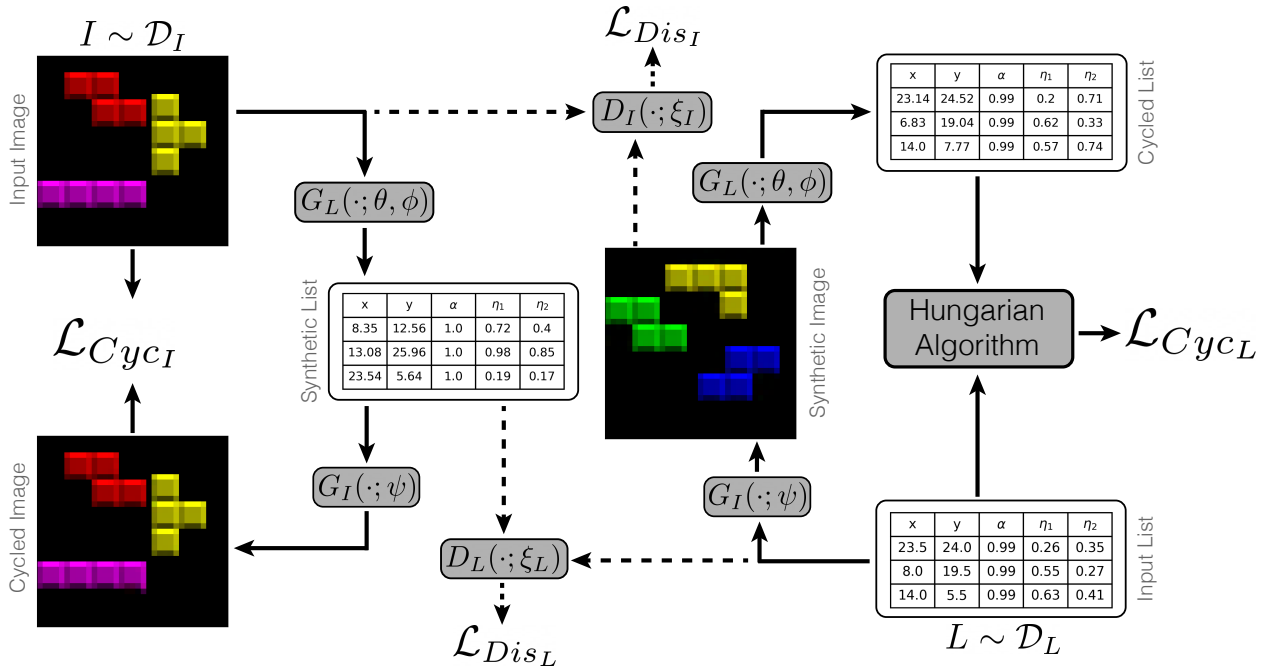


Figure 1: Model architecture and training losses. ORGAN is based on the Cycle-Consistent Generative Adversarial Network (cycleGAN) architecture Zhu et al. [2017], adapted to use an image (left) and a list (right) domain. Two GANs are used to transform between the two domains. By cycling through both generators, a cycle consist loss \mathcal{L}_{Cyc_L} and \mathcal{L}_{Cyc_I} can be enforced.

Usually, object-centric representation learning is done with VAEs. Popular representation learning approaches have been benchmarked by Yang and Yang Yang and Yang [2024]. In general, these approaches can be divided into spatial-attention models and scene-mixture models Lin et al. [2020]. For spatial-attention models, the location and object properties are explicitly modeled. Scene-mixture models, on the other hand, decompose a scene into multiple layers, where each pixel is assigned to one layer Greff et al. [2017], Engelcke et al. [2021]. The layers are also called slots Locatello et al. [2020]. Over time, object-centric representation learning has been curated such that it is now possible to learn representations of complex real-world data Seitzer et al. [2022].

GANs are another powerful tool for image generation. Given a dataset, a generator network learns to create new data samples such that they follow the same statistics of the training dataset. A discriminator network tries to distinguish between real and fake data and teaches the generator. Their focus lies in generating images as a composition of multiple objects Greff et al. [2020].

In addition to being used for directly inferring object representations, GANs have also been used to indirectly infer object properties. Of particular interest to us are Cycle-Consistent Generative Adversarial Networks (CycleGANs) Zhu et al. [2017], which consist of two separate GANs and two data domains. Each GAN transforms data from one domain to the other. In addition, there is a cycle consistency loss, which enforces that applying the generators of both GANs sequentially maps back to the original input. CycleGAN and its derivatives have been used for style transformations Brunner et al. [2018], Karras et al. [2019], Tmenova et al. [2019]. Since segmentation is a type of style transformation Thambawita et al. [2022], CycleGANs can also be used for segmentation in both a supervised Huo et al. [2018] and unsupervised environment Chen et al. [2018], Ihle et al. [2019]. The downside of these approaches is that they are not end-to-end, as they only segment the data but do not extract features directly.

Many object-centric representation learning approaches demonstrate their strength on benchmarks such as Pascal VOC Everingham et al. [2010] or MoVi Ghorbani et al. [2020]. Here, objects are large, visually distinctive, and embedded in complex, textured backgrounds. These settings allow for extra cues such as temporal continuity in video, strong background-foreground contrast, or semantic diversity. This helps object-centric representation learning methods to keep objects apart. In contrast, the datasets that motivate our work contain up to hundreds of small, nearly identical objects in low-contrast environments. Instance segmentation becomes challenging in such real-world conditions. In addition, real-world datasets contain richly textured backgrounds Seitzer et al. [2022].

For simplicity, this work attempts to instance segment real-world datasets with homogeneous backgrounds. Such datasets can, for example, be found particularly in microscopy images. Here, small objects are often overlooked, and visually similar but distinct objects may be incorrectly grouped. We will show that, as a result, existing architectures struggle to learn robust object-centric representations in such scenarios, which can be acquired by our approach. Furthermore, we show that CycleGANs correctly identify object counts even when test-time properties, such as object spacing and object count, differ from the training data.

The main contributions of this manuscript are:

- We propose a novel, fully differentiable CycleGAN framework, which mutually transforms an image and a list domain for unsupervised object-centric representation learning.
- We match state-of-the-art performance on synthetic datasets, while at the same time being the only approach that can reliably solve a more complex real-world dataset consisting of large sets of visually similar objects.
- We show that our method maintains its performance across different image dimensions, allowing a single trained model to scale without retraining.

2 Related Work

2.1 Generative Adversarial Networks

Generative Adversarial Networks (GANs) can be combined with lists (*i.e.* tables) Xu and Veeramachaneni [2018], Park et al. [2018]. These works have treated the entire dataset as a single large list. In contrast, our approach treats every object as a single entry in the list, making the entire list analogous to a single image rather than the full dataset.

CycleGANs were originally introduced for translating between two image domains Zhu et al. [2017]. Since then, CycleGAN architectures have been applied to other data modalities, such as sound Kaneko et al. [2019] and one-dimensional signals Easthope [2024]. Additionally, CycleGANs can facilitate cross-domain transfer. For instance, Gorti and Ma proposed a CycleGAN architecture capable of cross-modal transformations between text and images Gorti and Ma [2018].

2.2 Object-Centric Representation Learning

Previous work on object-centric representation learning using GANs focuses on image merging and segmentation. Various techniques have been proposed to extract object masks and separate them from the background Arandjelović and Zisserman [2019], Abdal et al. [2021] or to undo occlusion Kortylewski et al. [2021]. Another approach is object-wise image generation Van Steenkiste et al. [2020], where individual images are generated for each object and then aggregated. Models that explicitly encode transformation parameters for scene modification have also been proposed Nguyen-Phuoc et al. [2020], Ehrhardt et al. [2020]. Except for Ehrhardt et al. [2020], these models assume a fixed number of objects.

Spatial-attention models have been introduced by Eslami *et al.* through the Attend, Infer, Repeat (AIR) framework Eslami et al. [2016]. AIR recovers the objects iteratively using a recurrent neural network, which is intractable. Several derivatives exist that mitigate this problem by following a mean-field approach, such as GMAIR Zhu et al. [2022] and SPAIR Crawford and Pineau [2019], where an image is divided into subregions as proposed by YOLO and others Redmon [2016], Liu et al. [2016], Redmon [2018]. While these approaches are fast and scalable, their mean-field nature means that the recovered objects cannot be conditioned on each other. In addition, they struggle with objects that are larger than the subregion.

Slot attention-based models infer object slots through attention mechanisms Locatello et al. [2020]. SPACE Lin et al. [2020] combines a spatial attention model for the foreground with a scene-mixture model for the background. SLATE Singh et al. [2021] couples a slot-based encoder with a transformer decoder, while LSD Jiang et al. [2023] uses an unsupervised compositional conditional diffusion model that employs a latent diffusion framework conditioned on object slots. GOLD Chen et al. [2025] improves object-centric learning by disentangling intrinsic and extrinsic attributes. Scene-mixture models assign pixels to slots, ideally representing objects or background, but face the “slot-decoding dilemma” Singh et al. [2021], requiring iterative slot refinement Engelcke et al. [2021], Locatello et al. [2020], which is computationally expensive. SuPAIR Stelzner et al. [2019] addresses this with sum-product networks, while SPOT Kakogeorgiou et al. [2024] integrates self-training and sequence permutation strategies. To simplify slot extraction, SAMP Patil et al. [2024] employs convolutional and max pooling layers. Despite these advancements, models still struggle with highly textured objects Löwe et al. [2022], as well as small or numerous objects Kakogeorgiou et al. [2024]. Slot attention-based models tend to struggle with objects that have highly textured surfaces or intricate details Löwe et al. [2022], or when objects are small Kakogeorgiou et al. [2024] or too numerous.

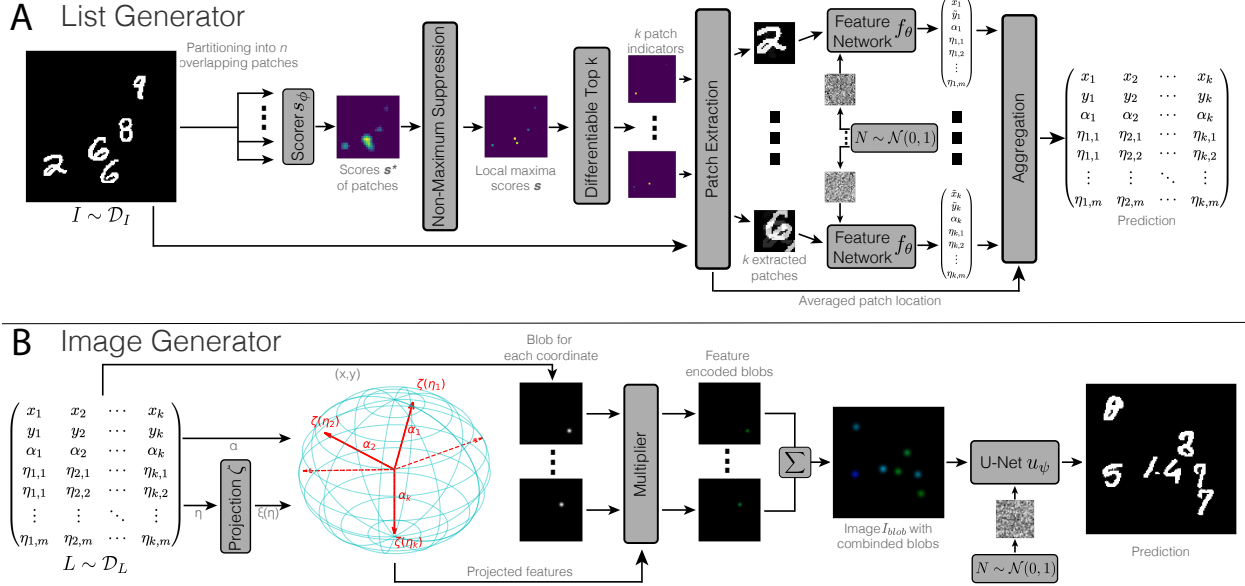


Figure 2: Network architectures used in this work. **(A)** List generator architecture, which transforms images into lists. First, the image is divided into patches and a score function is used, which predicts for each patch how likely it is to contain an object. After non-maximum suppression, a differentiable top-k operator detects k patches that contain objects. The feature network then extracts the object’s features. **(B)** Image generator architecture, which transforms lists into images. First, the list is transformed into an image based on its location and features. For that, each feature vector η_i is projected (ζ) onto a sphere, where the length of the projected vectors encodes α . Then, a similar approach as presented in BlobGAN is used Epstein et al. [2022] to convert the projections into an image. After adding a noise channel to allow for richer backgrounds, a U-net transforms the style of the image.

Another line of work has explored object discovery through information-theoretic principles. For instance, Wolf *et al.* proposed an inpainting-based segmentation model that minimizes information gain between partitions to segment densely packed cells in microscopy images Wolf et al. [2020]. More recently, complex-valued neural networks Löwe et al. [2022], inspired by the temporal correlation hypothesis from neuroscience, have emerged as a novel paradigm for object discovery. These models leverage complex-valued representations to capture temporal dependencies, offering an alternative to conventional segmentation approaches.

3 Methodology

Our model architecture is based on the CycleGAN Zhu et al. [2017]. CycleGANs learn a mapping between two different domains given unpaired training samples. In contrast to the original CycleGAN, which uses solely images, we work with two different data modalities. The goal is to convert an image $I \in \mathbb{R}^{h \times w \times c}$ to a list $L \in \mathbb{R}^{k \times (3+|\eta|)}$ and back by enforcing cycle-consistency. A list entry $l \in \mathbb{R}^{(3+|\eta|)}$ contains the x and y coordinates of an object, a scalar value a that indicates the probability that an object exists, and a feature vector η encoding object properties.

In addition, a generated list or image is shown to a modality-specific discriminator D_M , $M \in \{I, L\}$, where M is the image or list modality. The discriminator learns to distinguish between generated and real data. This adds a minimax game to the overall optimization problem, where the generator learns to fool the discriminator. The complete procedure is illustrated in Fig. 1.

3.1 Architecture

Since there are two different data modalities present, two separate generator architectures are required. Both generators are illustrated in Fig. 2A and Fig. 2B.

3.1.1 List Generator

The list generator $G_L(\cdot; \theta, \phi)$ maps I to L . This network consists of two key steps. In the first step, patches of interest are extracted. In the second step, the features of each object are predicted.

The list generator divides each image into n overlapping patches $p_i \in \mathbb{R}^{p_h \times p_w \times c}$ with a fixed stride. The patch size is chosen such that the biggest object of interest in the scene fits within. Overlapping the patches is crucial for a more precise location estimate. A scorer network s_ϕ then processes all patches in parallel. For each p_i , a score is returned that indicates the importance of the patch to be used for feature extraction. Due to the convolutional nature of s_ϕ , neighboring patches get a similar score. To mitigate the issue of marking patches for the same object multiple times with a high score, non-maximum suppression (NMS) is applied. The k patches of the highest interest are then extracted using an adapted differentiable top k algorithm Cordonnier et al. [2021]. Each of the top k patches is then independently processed by a convolutional feature network f_θ . A noise channel is incorporated in f_θ . This ensures D_L cannot exploit the fact that identical patches yield the same feature description. The feature network outputs one entry in the list for each patch. As the global position of the patch is unknown to the network, it can only determine the offset of the object relative to the patch’s center. The extracted offset is clipped to the stride of the initial partition. Then, the final location prediction is achieved by adding the patch location and the extracted offset.

Different from all other approaches presented in this work, our approach is independent of the image size. This allows us to train on small training images and generate lists for larger test images. The number of extracted patches k is a hyperparameter that can be tuned according to the maximum expected number of objects within an image.

3.1.2 Image Generator

The architecture of the image generator G_I is a modification of Epstein et al. [2022]. Unlike their approach, the mapping from our list L to the image $I_{blob} \in \mathbb{R}^{h \times w \times |\eta|}$ involves no learnable parameters. For each list entry l_i an equivalent isotropic Gaussian blob of fixed size is generated at the coordinates (x_i, y_i) . The image has $k + 1$ channels, which are created by projecting every η_i onto a unit sphere using the projection function $\zeta : [0, 1]^k \rightarrow \mathbb{R}^{k+1}$. The projection is then scaled by α_i :

$$I_{blob}(x, y, j) = \sum_i \alpha_i \zeta(\eta_{i,j}) e^{-\frac{(x-x_i)^2 + (y-y_i)^2}{2\sigma^2}}. \quad (1)$$

I_{blob} is then processed by a U-Net Ronneberger et al. [2015] u_ψ . An image has many more degrees of freedom, and hence its complexity is much greater than that of a list. To ensure that the image discriminator D_I cannot easily exploit this fact, u_ψ additionally receives a noise tensor.

3.1.3 Discriminators

To distinguish between synthetic and real images, a PatchGAN is used for the image discriminator D_I Zhu et al. [2017], Isola et al. [2017]. For the list discriminator D_L , two conditions are required: (1) Relations between elements have to be captured. (2) The ordering of list elements must have no effect. The first condition allows the approach to have feedback on inter-object relations. The latter is important, as a list describes the same scene irrespective of the order of its elements. To satisfy both conditions, a discriminator is introduced that incorporates an attention module Vaswani [2017]. The discriminator treats each object as a point in a point cloud. The described transformer architecture is a simplified version of the Point Transformer architecture by Zhao *et al.* Zhao et al. [2021] and described in the Supplementary Information.

3.2 Training

Both generators learn to map to an output that resembles a sample drawn from the target distribution \mathcal{D} by minimizing an adversarial loss \mathcal{L}_{Dis} Goodfellow et al. [2014]. The discriminator D_M tries to distinguish between synthetic and real samples and aims to maximize \mathcal{L}_{Dis} . For both modalities, the least squares approach as presented by Mao *et al.* was used Mao et al. [2017]. To enforce an invertible mapping, a cycle-consistency loss is introduced. The quality of a cycled image is assessed by calculating the mean absolute error (MAE) with respect to the input image. For the list cycle loss, an element-wise loss is defined. As the lists are unordered, a one-to-one assignment for each object between two lists is required. This task is known as the linear sum assignment problem. In this work, a modified version of the Jonker-Volgenant algorithm Jonker and Volgenant [1988], Crouse [2016] was implemented. The cost associated with a pair of elements depends on both the location and the probability of its presence:

$$\mathcal{C}_{Obj}(l_i, l_j) = \frac{\alpha_i}{W^2} \left\| \begin{pmatrix} x_i \\ y_i \end{pmatrix} - \begin{pmatrix} x_j \\ y_j \end{pmatrix} \right\|^2 + \lambda_{pres} (\alpha_i - \alpha_{Cyc_j})^2. \quad (2)$$

The scaling factor λ_{pres} ensures that for the comparison, object presence is of sufficient importance. A sorted list is then compared using the following loss function

$$\mathcal{L}_{Cycl} = \mathbf{E}_L \left\{ \frac{1}{k} \sum_l \left[C_{Obj}(l, l_{Cycl}) + \frac{\|\eta - \eta_{Cycl}\|^2}{|\eta|} \right] + \lambda_{loc} \frac{\|s_\phi(p) - t_p\|^2}{|t_p|} \right\}, \quad (3)$$

with t_p being the target for the scorer calculated from the locations of the objects. The second term serves as an additional gradient for s_ϕ . During training, it is crucial that s_ϕ extracts the right patches as quickly as possible.

Due to the two modalities, different weightings for losses of the list, image cycle, and adversarial losses are required. The loss function of the generator can be summarized as

$$\mathcal{L}_{Gen} = \lambda_{Dis_L} \mathcal{L}_{Dis_L} + \lambda_{Dis_I} \mathcal{L}_{Dis_I} + \lambda_{Cycl_I} \mathcal{L}_{Cycl_I} + \lambda_{Cycl_L} \mathcal{L}_{Cycl_L}, \quad (4)$$

where the first terms correspond to the adversarial losses of the two domains, and each lambda is a scalar value that weights the respective loss component. The hyperparameters for patch size p_h, p_w and the stride for patch extraction are adjusted according to the dataset used. In this work, the patch size is restricted to the case where $p_h = p_w$ and the stride is set to $\lfloor \frac{p_w}{8} \rfloor$ for simplicity. The σ which determines the size of generated blobs in G_I is fixed to $\frac{p_w}{10}$. To more effectively deal with objects on the boundary of the image, we optionally pad the input with n_{pad} pixels. In addition, the dimensionality of η depends on the specific dataset. All other hyperparameters are equivalent for all experiments. To enhance training stability, both discriminators employ a linear warm-up schedule for their learning rates and apply spectral normalization Miyato et al. [2018].

3.3 Datasets

We benchmark on four datasets (more details on datasets in Supplementary Information):

Tetrominoes Kbra et al. [2019]: 35×35 images with three non-overlapping tetrominoes of random colors and positions. The list has three entries.

Sprites: Up to ten colored sprites (squares–stars) on a 128×128 blue background, positions drawn with Poisson-disk sampling. The list has ten entries.

Multi-MNIST Deng [2012]: Up to ten handwritten digits per 128×128 image, possibly overlapping, locations are Poisson-disk sampled. The list has ten entries.

Cells Azmi [2023]: 128×128 microscope patches of blood containing many, visually similar, low-contrast cells. The list has ten entries.

4 Experiments

We compare ORGAN with four other recent approaches, where each covers a different technique used in unsupervised object-centric representation learning. SPACE Lin et al. [2020] is the most closely related to ORGAN as it is also spatial-attention based. At the same time, it incorporates a scene-mixture approach. Further, two slot-based models, LSD Jiang et al. [2023] and SLATE Singh et al. [2021] are presented. Finally, SPOT Kakogeorgiou et al. [2024], a self-supervised slot-based model with self-training and sequence permutations, has been trained for comparison. An ablation study of ORGAN can be found in Supplementary Information.

4.1 Qualitative Comparison

To qualitatively assess the performance of all models, their reconstructions were compared. In addition, the masks for the different slots or the bounding boxes around the center of the predicted objects were visualized. The results can be seen in Fig. 3.

ORGAN gives a detailed reconstruction of the input images. In addition, it manages to precisely detect most objects across all four datasets.

SPACE shows accurate reconstructions for the synthetic datasets. It reliably detects separate objects in *Sprites* and *Multi-MNIST*. For *Tetrominoes*, it assigns certain tetrominoes (in our case, red ones) to the background. For *Cells*, SPACE fails to detect any cell as an object, resulting in reconstructions generated solely by its background module. The low contrast of the dataset makes it difficult to separate the back- and foreground.

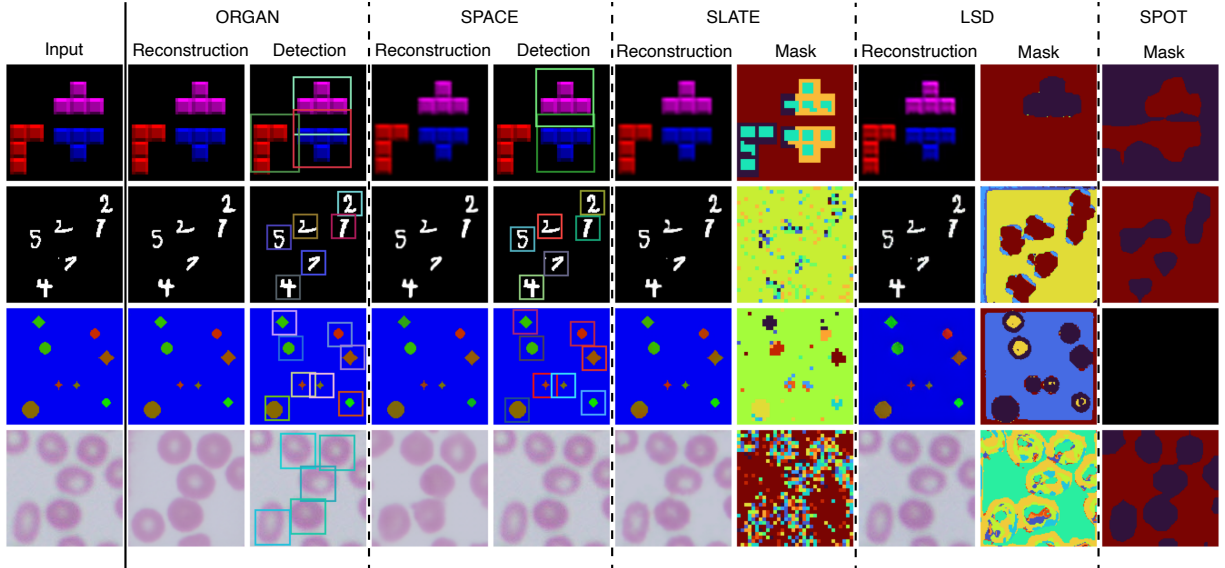


Figure 3: Examples of object detection performance for four different datasets. We show performance for ORGAN (ours), SPACE Lin et al. [2020], SLATE Singh et al. [2021], LSD Jiang et al. [2023] and SPOT Kakogeorgiou et al. [2024]. We present both the reconstruction as well as the object detection in the form of fixed bounding boxes for ORGAN and SPACE. The color code of the bounding box represents the extracted feature vector. For SLATE, LSD, and SPOT we present the recovered slot masks (color-coded). SPOT does not allow for image reconstruction.

Table 1: F1-scores (in %) and training/inference times (hours/ms) for all models on 128×128 images.

Method	Tetrominoes		MNIST		Sprites		Cells	
	F1	Train/Infer	F1	Train/Infer	F1	Train/Infer	F1	Train/Infer
ORGAN	89.2±20.5	44.0 / 2.5	86.1±3.9	39.0 / 3.5	88.1±2.3	36.0 / 4.0	77.9±8.6	31.5 / 3.4
SPACE	76.0±15.7	13.5 / 17.8	88.7±4.7	16.5 / 15.0	88.5±4.3	4.08 / 29.6	0.0±0.0	13.0 / 15.0
SLATE	30.3±24.8	6.75 / 3.4	5.8±7.6	0.75 / 3.4	12.4±10.6	0.75 / 3.0	46.6±9.3	0.75 / 3.5
LSD	20.0±39.8	7.5 / 8.0	5.7±28.0	16.0 / 4.0	6.4±17.7	11.5 / 7.0	53.9±11.9	10.5 / 7.0
SPOT	13.8±44.6	10.0 / 37.5	5.2±43.0	10.0 / 36.3	0.5±21.2	10.0 / 32.8	24.8±0.0	10.0 / 32.8

SLATE achieves precise reconstructions across all datasets but inferior mask assignments, as separate objects are assigned to the same slots. For example, in *Tetrominoes*, it separates the block boundaries from its centers. The model even allocates multiple slots to a single object without unique associations, as is done in *Sprites*. In addition, for *Cells* and *Multi-MNIST*, the segmentation yields only limited structural detail.

LSD separates the foreground from the background across all synthetic datasets. However, in most cases, it assigns all distinct objects to a single slot while reserving another slot for the background. In the *Sprites* dataset, LSD partially succeeds in separating green objects while merging those of other colors into the same slot. In contrast, in the *Cells* dataset, LSD struggles to distinguish the foreground from the background, likely because the cell centers share the same color as the background, leading to their misallocation as part of it.

SPOT demonstrates the ability to separate foreground from background in most datasets; however, its masks appear coarser than those produced by other models. The model is most challenged by the *Sprites* dataset, which consists of multiple small objects. Here, SPOT over-segmented the region, failing to isolate individual objects. Instead of assigning distinct slots to separate objects, SPOT tends to merge multiple entities into a single slot. As shown in the Supplementary Information, this behavior is likely due to the encoder’s slot-attention mechanism, which struggles to generate sufficiently distinct slot representations.

4.2 Quantitative Comparison

The models were quantitatively evaluated using the F1-score for object detection accuracy, along with measurements of training and inference time (Table 1). For SLATE, LSD, and SPOT, object locations were extracted as the center of mass

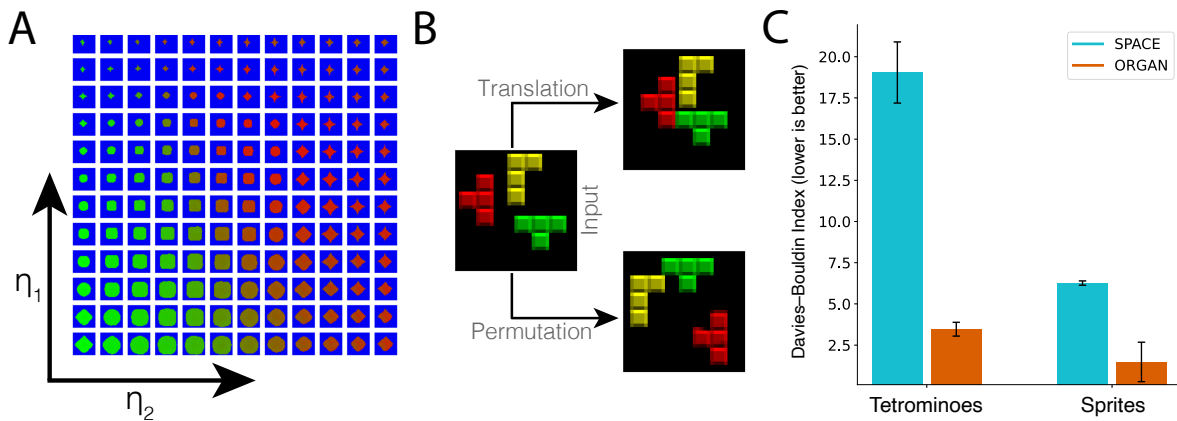


Figure 4: Latent space quality of ORGAN. (A) The latent space as encoded by η is presented for the *Sprites* dataset. Two of the three dimensions are plotted. The third dimension is kept fixed at its center. The feature space encodes the color, shape, and size of the object. (B) An input image of the *Tetrominoes* dataset is cycled, while the list elements are modified. Top: All objects were moved closer to the center. Bottom: The object properties were swapped between the three objects counterclockwise. (C) To compare how well object clustering works on the feature space, the Davies–Bouldin Index Davies and Bouldin [1979] was calculated for the two tested approaches, which detected distinct objects for *Sprites* and *Tetrominoes*; ORGAN and SPACE. Our method achieves superior separability.

of each slot’s segmentation mask. For the Cells dataset, 50 images were annotated by an expert to provide ground-truth object positions. All training and inference experiments were conducted on an NVIDIA RTX 2080 Ti GPU. Across all presented datasets, the evaluated slot-based models (SLATE, LSD, SPOT) do not reliably detect distinct objects. In contrast, SPACE and ORGAN achieve substantially higher detection performance. While SPACE trains more than twice as fast as ORGAN, inference with ORGAN is approximately five times faster. Since only SPACE and ORGAN consistently detect distinct objects, subsequent experiments are restricted to these two models.

4.3 Expressiveness of Feature Space

The *Sprites* dataset was generated using a three-dimensional feature vector where each dimension corresponds to either color, scale, or shape. Therefore, it is possible to contrast the true feature space to the feature space of ORGAN. A two-dimensional slice through the feature space is shown in Fig. 4A. The feature space shows changes in object size, shape, and color. The feature space shows that ORGAN is capable of disentangling the location and object properties. This capability is further demonstrated in Fig. 4B, where an input image of *Tetrominoes* is first transformed into a list, then the list is modified, and finally cycled back into an image.

We were further interested in how consistently similar objects are placed within the extracted feature space. For this, we used a modified *Sprites* dataset with three shapes, colors, and sizes (27 object types), as well as the *Tetrominoes* dataset. Feature vectors were grouped by object type, and group separability was assessed using the Davies–Bouldin Index Davies and Bouldin [1979]. Results are shown in Fig. 4C, where ORGAN significantly outperforms SPACE, indicating a more structured and separable feature space.

4.4 Detection Accuracy in Large Scenes

In order to investigate how well ORGAN works on images of different sizes and with many more objects than present during training, we trained it on the standard *Sprites* dataset with an image size of 128×128 pixels. Here, only models that exhibited sustained improvements in cycle loss by the 100th epoch were retained (acceptance rate: 75 %). ORGAN was evaluated on a new dataset of size 256×256 with up to 39 objects. Network performance was measured using precision and recall metrics. The results are shown in Fig. 5A. SPACE was used to compare the performance of our architecture. As SPACE does not allow for images of different sizes for training and prediction, it was trained directly on 256×256 inputs.

When comparing precision and recall for SPACE and ORGAN (see Fig. 5A), no distinction between the two models can be made when only a few objects are present. However, as the number of objects in an image increases, the recall metric

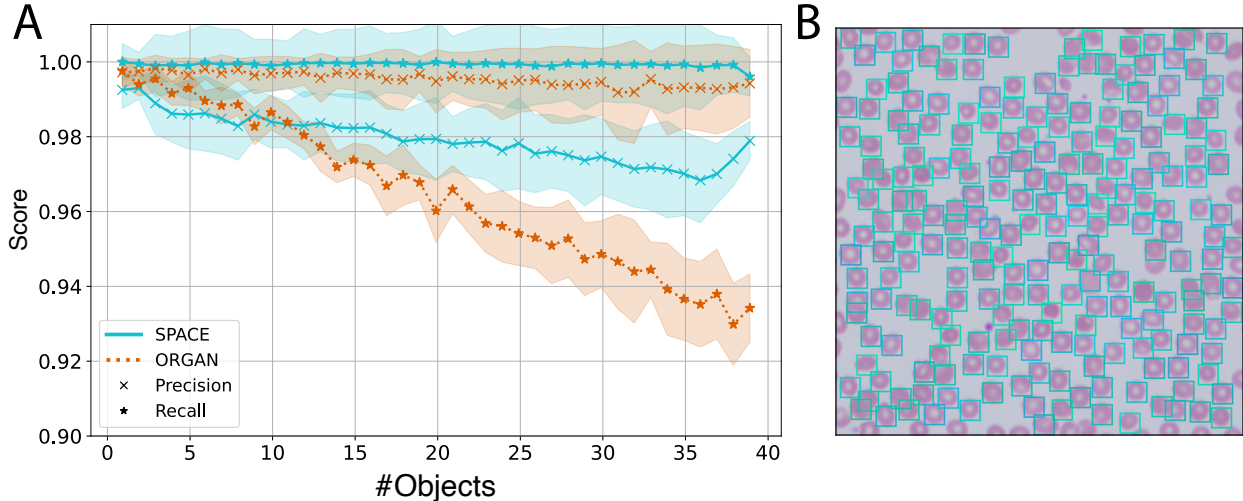


Figure 5: Analysis of the generalization capabilities of the object detection accuracy. **A** Recall and precision are plotted for both ORGAN and SPACE for *Sprites*. The architecture of SPACE can only be applied to a fixed input size (here 256×256). ORGAN was trained on 128×128 and applied to 256×256 . This approach benefits SPACE. Yet, ORGAN outperforms in precision, while SPACE has a higher recall. **(B)** ORGAN can also generalize to much larger images. Trained on patches of size 128×128 , prediction results on a 768×768 image of the *Cells* dataset are presented. The color code of the bounding box illustrates differences in extracted features η .

drops for ORGAN (recall at 39 objects for ORGAN: 0.934, SPACE: 0.996). Still, ORGAN outperformed ORGAN across the board when considering the precision metric (at 39 objects for ORGAN: 0.994, SPACE: 0.979).

To further evaluate ORGAN on real-world applications, it was trained for *Cells* with images containing 128×128 pixels and tested on a large image of 768×768 pixels. The result is shown in Fig. 5B. Ground truth was established from annotations by three experts. Three experts provided the ground-truth annotations, with an inter-annotator F1 of 0.977; the model scored an average F1 of 0.750 compared to the experts. This test illustrates the strong generalization capabilities of ORGAN. The small patches seen during training contain partially cut-off cells on the boundary. Irrespectively, the approach does not seem affected by this shortcoming of the training data and successfully captures a broader scene.

When models are restricted to a fixed input size, input images are usually sliced into multiple, potentially overlapping parts. As our model allows us to scale to different input sizes regardless of the size of the image during training, the need to slice large inputs is unnecessary. This is beneficial, as slicing has an inherent problem of boundary effects.

5 Conclusion

Our approach was the only one tested that detected separate entities on a low-contrast image of cells. We showed that the learned feature mapping allows for an easier distinction of different object types compared with non-GAN approaches like SPACE. We attribute these performance gains to two key factors: First, GANs produce sharper reconstructions compared to VAEs Wang et al. [2021]; second, the cyclic architecture of ORGAN provides additional training feedback for the generators, which can be effectively leveraged. Hence, our approach effectively addresses a common criticism of object-centric representation learning: the purported inability of GAN-based methods to handle large numbers of objects Yang and Yang [2022, 2024].

Debate persists over whether object slots should be conditioned on previously recovered objects. Crawford and Pineau add such a condition to prevent duplicate detections, but it is intractable and scales poorly Crawford and Pineau [2019]. SPACE replaces it with a mean-field, parallel detector that is more scalable yet ignores inter-object dependencies Lin et al. [2020]. ORGAN sidesteps both issues: a differentiable top-k locator yields tractable proposals, while the GAN discriminator—with self-attention and non-maximum suppression—penalises duplicates, letting slots remain mutually dependent Vaswani [2017]. This combination keeps the model scalable without the weight-growth or sequential bottlenecks that hamper current approaches.

Despite its effectiveness, ORGAN has several limitations. Like many other GAN-based architectures, ORGAN can be inherently unstable during training and care needs to be taken during the minimax optimization of the GANs. In addition, ORGAN does not aim to reconstruct complex backgrounds and may therefore struggle with datasets that have such backgrounds. Furthermore, the patch-based approach means that processing any object larger than a patch, or two objects that lie too close together across a patch boundary, may be missed. Finally, ORGAN requires a dataset that contains lists, where the size is controlled by a hyperparameter. This hyperparameter is unique to ORGAN and needs tuning.

Acknowledgements

This research was supported by ETH Zürich, the Swiss National Science Foundation (SNSF) [project number 10.001.282], and the Swiss Data Science Center (SDSC). The authors also thank Peter Littlewood and János Vörös for their continued support. S. J. Ihle is supported by the Eric and Wendy Schmidt AI in Science Fellowship, a program of Schmidt Sciences.

Availability Statement

All code is freely available on GitHub: <https://github.com/Hullimulli/ORGAN>.

References

- Adeel Pervez, Phillip Lippe, and Efstratios Gavves. Differentiable mathematical programming for object-centric representation learning. *arXiv preprint arXiv:2210.02159*, 2022.
- Francesco Locatello, Dirk Weissenborn, Thomas Unterthiner, Aravindh Mahendran, Georg Heigold, Jakob Uszkoreit, Alexey Dosovitskiy, and Thomas Kipf. Object-centric learning with slot attention. *Advances in neural information processing systems*, 33:11525–11538, 2020.
- Jun-Yan Zhu, Taesung Park, Phillip Isola, and Alexei A Efros. Unpaired image-to-image translation using cycle-consistent adversarial networks. In *Proceedings of the IEEE international conference on computer vision*, pages 2223–2232, 2017.
- Peter W Battaglia, Jessica B Hamrick, and Joshua B Tenenbaum. Simulation as an engine of physical scene understanding. *Proceedings of the National Academy of Sciences*, 110(45):18327–18332, 2013.
- Brenden M Lake, Tomer D Ullman, Joshua B Tenenbaum, and Samuel J Gershman. Building machines that learn and think like people. *Behavioral and brain sciences*, 40:e253, 2017.
- James R Kubricht, Keith J Holyoak, and Hongjing Lu. Intuitive physics: Current research and controversies. *Trends in cognitive sciences*, 21(10):749–759, 2017.
- Elizabeth S Spelke, Karen Breinlinger, Janet Macomber, and Kristen Jacobson. Origins of knowledge. *Psychological review*, 99(4):605, 1992.
- David Mascharka, Philip Tran, Ryan Soklaski, and Arjun Majumdar. Transparency by design: Closing the gap between performance and interpretability in visual reasoning. In *Proceedings of the IEEE conference on computer vision and pattern recognition*, pages 4942–4950, 2018.
- Constantine P Papageorgiou, Michael Oren, and Tomaso Poggio. A general framework for object detection. In *Sixth international conference on computer vision (IEEE Cat. No. 98CH36271)*, pages 555–562. IEEE, 1998.
- Margrit Betke and Nicholas C Makris. Fast object recognition in noisy images using simulated annealing. In *Proceedings of IEEE International Conference on Computer Vision*, pages 523–530. IEEE, 1995.
- Diederik P Kingma. Auto-encoding variational bayes. *arXiv preprint arXiv:1312.6114*, 2013.
- Ian Goodfellow, Jean Pouget-Abadie, Mehdi Mirza, Bing Xu, David Warde-Farley, Sherjil Ozair, Aaron Courville, and Yoshua Bengio. Generative adversarial nets. *Advances in neural information processing systems*, 27, 2014.
- Thomas Kipf, Elise Van der Pol, and Max Welling. Contrastive learning of structured world models. *arXiv preprint arXiv:1911.12247*, 2019.
- Yafei Yang and Bo Yang. Benchmarking and analysis of unsupervised object segmentation from real-world single images. *International Journal of Computer Vision*, 132(6):2077–2113, 2024.
- Zhixuan Lin, Yi-Fu Wu, Skand Vishwanath Peri, Weihao Sun, Gautam Singh, Fei Deng, Jindong Jiang, and Sungjin Ahn. Space: Unsupervised object-oriented scene representation via spatial attention and decomposition. *arXiv preprint arXiv:2001.02407*, 2020.

-
- Klaus Greff, Sjoerd Van Steenkiste, and Jürgen Schmidhuber. Neural expectation maximization. *Advances in Neural Information Processing Systems*, 30, 2017.
- Martin Engelcke, Oiwi Parker Jones, and Ingmar Posner. Genesis-v2: Inferring unordered object representations without iterative refinement. *Advances in Neural Information Processing Systems*, 34:8085–8094, 2021.
- Maximilian Seitzer, Max Horn, Andrii Zadaianchuk, Dominik Zietlow, Tianjun Xiao, Carl-Johann Simon-Gabriel, Tong He, Zheng Zhang, Bernhard Schölkopf, Thomas Brox, et al. Bridging the gap to real-world object-centric learning. *arXiv preprint arXiv:2209.14860*, 2022.
- Klaus Greff, Sjoerd Van Steenkiste, and Jürgen Schmidhuber. On the binding problem in artificial neural networks. *arXiv preprint arXiv:2012.05208*, 2020.
- Gino Brunner, Yuyi Wang, Roger Wattenhofer, and Sumu Zhao. Symbolic music genre transfer with cyclegan. In *2018 IEEE 30th international conference on tools with artificial intelligence (ictai)*, pages 786–793. IEEE, 2018.
- Tero Karras, Samuli Laine, and Timo Aila. A style-based generator architecture for generative adversarial networks. In *Proceedings of the IEEE/CVF conference on computer vision and pattern recognition*, pages 4401–4410, 2019.
- Oleksandra Tmenova, Rémi Martin, and Luc Duong. Cyclegan for style transfer in x-ray angiography. *International journal of computer assisted radiology and surgery*, 14:1785–1794, 2019.
- Vajira Thambawita, Pegah Salehi, Sajad Amouei Sheshkal, Steven A Hicks, Hugo L Hammer, Sravanthi Parasa, Thomas de Lange, Pål Halvorsen, and Michael A Riegler. Singan-seg: Synthetic training data generation for medical image segmentation. *PLoS one*, 17(5):e0267976, 2022.
- Yuankai Huo, Zhoubing Xu, Shunxing Bao, Albert Assad, Richard G Abramson, and Bennett A Landman. Adversarial synthesis learning enables segmentation without target modality ground truth. In *2018 IEEE 15th international symposium on biomedical imaging (ISBI 2018)*, pages 1217–1220. IEEE, 2018.
- Cheng Chen, Qi Dou, Hao Chen, and Pheng-Ann Heng. Semantic-aware generative adversarial nets for unsupervised domain adaptation in chest x-ray segmentation. In *Machine Learning in Medical Imaging: 9th International Workshop, MLMI 2018, Held in Conjunction with MICCAI 2018, Granada, Spain, September 16, 2018, Proceedings 9*, pages 143–151. Springer, 2018.
- Stephan J Ihle, Andreas M Reichmuth, Sophie Girardin, Hana Han, Flurin Stauffer, Anne Bonnin, Marco Stampanoni, Karthik Pattisapu, János Vörös, and Csaba Forró. Unsupervised data to content transformation with histogram-matching cycle-consistent generative adversarial networks. *Nature Machine Intelligence*, 1(10):461–470, 2019.
- Mark Everingham, Luc Van Gool, Christopher KI Williams, John Winn, and Andrew Zisserman. The pascal visual object classes (voc) challenge. *International journal of computer vision*, 88:303–338, 2010.
- Saeed Ghorbani, K Mahdaviani, Anne Thaler, K Kording, DJ Cook, G Blohm, and NF Troje. Movi: A large multipurpose motion and video dataset. *arXiv 2020. arXiv preprint arXiv:2003.01888*, 9, 2020.
- Lei Xu and Kalyan Veeramachaneni. Synthesizing tabular data using generative adversarial networks. *arXiv preprint arXiv:1811.11264*, 2018.
- Noseong Park, Mahmoud Mohammadi, Kshitij Gorde, Sushil Jajodia, Hongkyu Park, and Youngmin Kim. Data synthesis based on generative adversarial networks. *arXiv preprint arXiv:1806.03384*, 2018.
- Takuhiro Kaneko, Hirokazu Kameoka, Kou Tanaka, and Nobukatsu Hojo. Cyclegan-vc2: Improved cyclegan-based non-parallel voice conversion. In *ICASSP 2019-2019 IEEE International Conference on Acoustics, Speech and Signal Processing (ICASSP)*, pages 6820–6824. IEEE, 2019.
- Eric Easthope. (un) paired signal-to-signal translation with 1d conditional gans. *arXiv preprint arXiv:2403.04800*, 2024.
- Satya Krishna Gorti and Jeremy Ma. Text-to-image-to-text translation using cycle consistent adversarial networks. *arXiv preprint arXiv:1808.04538*, 2018.
- Relja Arandjelović and Andrew Zisserman. Object discovery with a copy-pasting gan. *arXiv preprint arXiv:1905.11369*, 2019.
- Rameen Abdal, Peihao Zhu, Niloy J Mitra, and Peter Wonka. Labels4free: Unsupervised segmentation using stylegan. In *Proceedings of the IEEE/CVF International Conference on Computer Vision*, pages 13970–13979, 2021.
- Adam Kortylewski, Ju He, Qing Liu, Christian Cosgrove, Chenglin Yang, and Alan L Yuille. Compositional generative networks and robustness to perceptible image changes. In *2021 55th Annual Conference on Information Sciences and Systems (CISS)*, pages 1–8. IEEE, 2021.
- Sjoerd Van Steenkiste, Karol Kurach, Jürgen Schmidhuber, and Sylvain Gelly. Investigating object compositionality in generative adversarial networks. *Neural Networks*, 130:309–325, 2020.

-
- Thu H Nguyen-Phuoc, Christian Richardt, Long Mai, Yongliang Yang, and Niloy Mitra. Blockgan: Learning 3d object-aware scene representations from unlabelled images. *Advances in neural information processing systems*, 33: 6767–6778, 2020.
- Sébastien Ehrhardt, Oliver Groth, Aron Monszpart, Martin Engelcke, Ingmar Posner, Niloy Mitra, and Andrea Vedaldi. Relate: Physically plausible multi-object scene synthesis using structured latent spaces. *Advances in Neural Information Processing Systems*, 33:11202–11213, 2020.
- SM Eslami, Nicolas Heess, Theophane Weber, Yuval Tassa, David Szepesvari, Geoffrey E Hinton, et al. Attend, infer, repeat: Fast scene understanding with generative models. *Advances in neural information processing systems*, 29, 2016.
- Weijin Zhu, Yao Shen, Mingqian Liu, and Lizeth Patricia Aguirre Sanchez. Gmair: Unsupervised object detection based on spatial attention and gaussian mixture model. *Computational Intelligence and Neuroscience*, 2022(1): 7254462, 2022.
- Eric Crawford and Joelle Pineau. Spatially invariant unsupervised object detection with convolutional neural networks. In *Proceedings of the AAAI Conference on Artificial Intelligence*, volume 33, pages 3412–3420, 2019.
- J Redmon. You only look once: Unified, real-time object detection. In *Proceedings of the IEEE conference on computer vision and pattern recognition*, 2016.
- Wei Liu, Dragomir Anguelov, Dumitru Erhan, Christian Szegedy, Scott Reed, Cheng-Yang Fu, and Alexander C Berg. Ssd: Single shot multibox detector. In *Computer Vision—ECCV 2016: 14th European Conference, Amsterdam, The Netherlands, October 11–14, 2016, Proceedings, Part I 14*, pages 21–37. Springer, 2016.
- Joseph Redmon. Yolov3: An incremental improvement. *arXiv preprint arXiv:1804.02767*, 2018.
- Gautam Singh, Fei Deng, and Sungjin Ahn. Illiterate dall-e learns to compose. *arXiv preprint arXiv:2110.11405*, 2021.
- Jindong Jiang, Fei Deng, Gautam Singh, and Sungjin Ahn. Object-centric slot diffusion, 2023. URL <https://arxiv.org/abs/2303.10834>.
- Tianyang Chen, Yufei Huang, Zhiqiang Shen, Jian Zhang, Yao Li, and Lei Zhang. Learning global object-centric representations via disentangled slot attention. *Machine Learning*, 114(40):1–22, 2025. doi:10.1007/s10994-024-06687-9.
- Karl Stelzner, Robert Peharz, and Kristian Kersting. Faster attend-infer-repeat with tractable probabilistic models. In *International Conference on Machine Learning*, pages 5966–5975. PMLR, 2019.
- Ioannis Kakogeorgiou, Spyros Gidaris, Konstantinos Karantzalos, and Nikos Komodakis. Spot: Self-training with patch-order permutation for object-centric learning with autoregressive transformers. In *Proceedings of the IEEE/CVF Conference on Computer Vision and Pattern Recognition*, pages 22776–22786, 2024.
- Vihang Patil, Andreas Radler, Daniel Klotz, and Sepp Hochreiter. Simplified priors for object-centric learning, 2024. URL <https://arxiv.org/abs/2410.00728>.
- Sindy Löwe, Phillip Lippe, Maja Rudolph, and Max Welling. Complex-valued autoencoders for object discovery. *arXiv preprint arXiv:2204.02075*, 2022.
- Steffen Wolf, Fred A Hamprecht, Jan Funke, HHMI Janelia, and VA Ashburn. Inpainting networks learn to separate cells in microscopy images. In *BMVC*, 2020.
- Dave Epstein, Taesung Park, Richard Zhang, Eli Shechtman, and Alexei A Efros. Blobgan: Spatially disentangled scene representations. In *European Conference on Computer Vision*, pages 616–635. Springer, 2022.
- Jean-Baptiste Cordonnier, Aravindh Mahendran, Alexey Dosovitskiy, Dirk Weissenborn, Jakob Uszkoreit, and Thomas Unterthiner. Differentiable patch selection for image recognition. In *Proceedings of the IEEE/CVF Conference on Computer Vision and Pattern Recognition*, pages 2351–2360, 2021.
- Olaf Ronneberger, Philipp Fischer, and Thomas Brox. U-net: Convolutional networks for biomedical image segmentation. In *Medical image computing and computer-assisted intervention—MICCAI 2015: 18th international conference, Munich, Germany, October 5-9, 2015, proceedings, part III 18*, pages 234–241. Springer, 2015.
- Phillip Isola, Jun-Yan Zhu, Tinghui Zhou, and Alexei A Efros. Image-to-image translation with conditional adversarial networks. In *Proceedings of the IEEE conference on computer vision and pattern recognition*, pages 1125–1134, 2017.
- A Vaswani. Attention is all you need. *Advances in Neural Information Processing Systems*, 2017.
- Hengshuang Zhao, Li Jiang, Jiaya Jia, Philip HS Torr, and Vladlen Koltun. Point transformer. In *Proceedings of the IEEE/CVF international conference on computer vision*, pages 16259–16268, 2021.

-
- Xudong Mao, Qing Li, Haoran Xie, Raymond YK Lau, Zhen Wang, and Stephen Paul Smolley. Least squares generative adversarial networks. In *Proceedings of the IEEE international conference on computer vision*, pages 2794–2802, 2017.
- Roy Jonker and Ton Volgenant. A shortest augmenting path algorithm for dense and sparse linear assignment problems. In *DGOR/NSOR: Papers of the 16th Annual Meeting of DGOR in Cooperation with NSOR/Vorträge der 16. Jahrestagung der DGOR zusammen mit der NSOR*, pages 622–622. Springer, 1988.
- David F Crouse. On implementing 2d rectangular assignment algorithms. *IEEE Transactions on Aerospace and Electronic Systems*, 52(4):1679–1696, 2016.
- Takeru Miyato, Toshiki Kataoka, Masanori Koyama, and Yuichi Yoshida. Spectral normalization for generative adversarial networks. *arXiv preprint arXiv:1802.05957*, 2018.
- Rishabh Kabra, Chris Burgess, Loic Matthey, Raphael Lopez Kaufman, Klaus Greff, Malcolm Reynolds, and Alexander Lerchner. Multi-object datasets. <https://github.com/deepmind/multi-object-datasets/>, 2019.
- Li Deng. The mnist database of handwritten digit images for machine learning research [best of the web]. *IEEE signal processing magazine*, 29(6):141–142, 2012.
- Irfan Bin Azmi. Blood dataset. 2024-07-08. url: <https://www.kaggle.com/datasets/irfanbinazmi/blood-dataset>, 2023.
- David L Davies and Donald W Bouldin. A cluster separation measure. *IEEE transactions on pattern analysis and machine intelligence*, (2):224–227, 1979.
- Zhengwei Wang, Qi She, and Tomas E Ward. Generative adversarial networks in computer vision: A survey and taxonomy. *ACM Computing Surveys (CSUR)*, 54(2):1–38, 2021.
- Yafei Yang and Bo Yang. Promising or elusive? unsupervised object segmentation from real-world single images. *Advances in Neural Information Processing Systems*, 35:4722–4735, 2022.